Title

Revealing the infiltration process and retention mechanisms of surface applied free DNA tracer through soil under flood irrigation

Authors

Liu, Geng
Guo, Linxi
Wang, Chaozi
et al.

Publication Date

2023-12-01

DOI

10.1016/j.scitotenv.2023.167378

Revealing the adsorption mechanisms of free DNA tracer through real soil under flood irrigation

Geng Liu[a,1], Linxi Guo[a,1], Chaozi Wang[a,], Jiarong Liu[a], Zengjie Hu[a], Helen E. Dahlke[b], En Xie[a], Xiao Zhao[a], Guanhua Huang[a], Jun Niu[a], Keyu Fa[a], Chenglong Zhang[a], Zailin Huo[a]*

[*] Corresponding author: Chaozi Wang, E-mail: chaoziwang@cau.edu.cn

[1] Geng Liu and Linxi Guo contribute equally to this work.

[a] College of Water Resources and Civil Engineering, China Agricultural University, Beijing 100083, China

[b] Department of Land, Air, and Water Resources, University of California, Davis, Davis, CA 95616, USA

Abstract

Wang et al. (2022) recently demonstrated that free DNA tracers have the potential in tracing water flow and contaminant transport through the vadose zone. However, it is still unclear what are the adsorption/desorption rates of free DNA tracer in real soil and what are the dominant mechanisms controlling these rates? To answer these questions, we tested the fate and transport behavior of free DNA tracers through packed sandy soil columns. From the experimental breakthrough curves and by fitting a two-site kinetic sorption model adsorption/desorption rates could be obtained and tracer retention profiles could be simulated. Together these results revealed that 1) the adsorption of free DNA was dominantly to clay particles in the real soil, which took up 1.96 % by

volume, but took up much more than 97.70 % by surface area; and 2) at a pore water pH of 8.0, excluding the 4.9 % passing through and 3.1 % degradation amount, the main retention mechanisms in the experimental soil were ligand exchange (42.0 %), Van der Waals interactions (mainly hydrogen bonds) electrostatic forces and straining (together 44.7 %), and cation bridge (5.3 %). To our knowledge, this study is the first to reveal the adsorption mechanisms of free synthetic DNA tracers passing through real soil. The adsorption mechanisms of free DNA tracer in real soil revealed here could facilitate the application of free DNA tracer to trace vadose zone water flow and solute/ contaminant transport under flood irrigation and other infiltration conditions.

Keywords: free DNA tracer, real soil, adsorption, ligand exchange, cation bridge, hydrogen bond, electrostatic force

1. Introduction

Although DNA tracers, either free DNA strands or DNA strands encapsulated by polymers or silica for protection, have unparalleled advantage in tracking the connectivity between multiple sources and multiple sinks at a very low detection limit (Wang et al., 2023). However, the application of DNA tracers to real soil systems is still at a pioneer stage due to the fast degradation (Sirois and Buckley, 2019) and strong adsorption (Pang et al., 2022) of free DNA tracers in real soil and the high retention of encapsulated DNA tracers in real soil (Wang et al., 2019). Encapsulated DNA tracers could hardly transport through packed soil without preferential pathways (Wang et al., 2019); whereas, free DNA tracers have recently been proven through both experiments and model simulations to be relatively mobile in packed real soil textured porous media (Wang et al., 2022).

However, little is still known about how free DNA tracers behave in real soil. Specifically, what are the adsorption/desorption rates of free synthetic DNA in real soil and what are the dominant mechanisms controlling these rates? Generally, the dominant adsorption mechanisms of naturally occurring DNA to clay minerals include electrostatic forces, Van der Waals interactions (mainly hydrogen bond), ligand exchange and cation bridge (Yu et al., 2013). The isoelectric point (pI) of DNA is around 5 (Sodnikar et al., 2021), which means that at a pH>5.0, DNA is negatively charged (Xue and Feng, 2018) and would not be directly adsorbed to negatively charged minerals by electrostatic force (Cai et al., 2006). However, at pH>5.0 the negatively charged DNA could adsorb to positively charged minerals, for instance, minerals containing Al_2O_3 and Fe_2O_3 (Zhang et al., 2021) (Figure 1a). The polar DNA molecules can be adsorbed on the corner or broken edges of clay minerals which are phyllosilicates (Yu et al., 2013). Because phyllosilicates possess amphoteric hydroxyl groups on their broken surfaces (Gardner and Gunsch, 2017) which can form hydrogen bonds (Scholes et al., 2011) (Figure 1b). Ligand exchange refers to the direct binding of phosphate groups at the two ends of the DNA molecule to the hydroxyl groups on the edges of clay minerals (Pedreira-Segade et al., 2018) (Figure 1c). Thus, the presence of free phosphate in pore water may affect the adsorption and binding of DNA onto clay minerals (Saeki et al., 2011a; Saeki et al., 2010). Cation bridges form when multivalent cations, particularly, divalent cations, such as Ca^{2+} and Mg^{2+} attract the negatively charged phosphate groups of the DNA molecule on one hand and grab the negatively charged tetrahedral silica layer on the clay surface on the other hand (Sheng et al., 2019) (Figure 1d). Thus, chelating multivalent cations with strong chelation, e.g., EDTA, could break the cation bridges and release cation-bridge-bonded DNA molecules (Bulushev et al., 2014; Liang and Keeley, 2013).

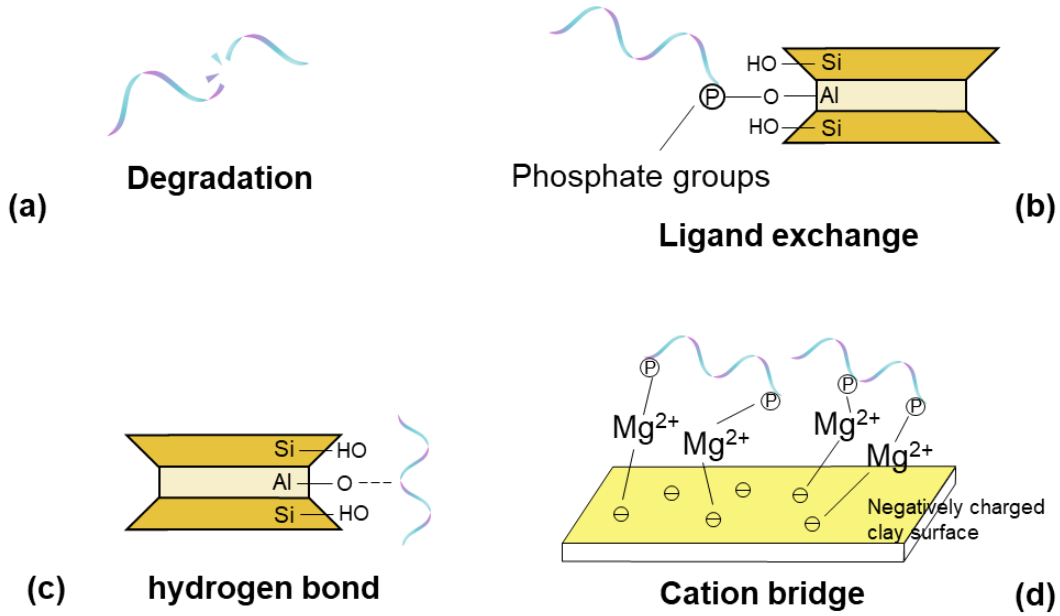

Figure 1. Retention and degradation mechanisms controlling the transport of free DNA through real soil: (a) degradation, (b) Ligand exchange, (c) Van der Waals interactions, (d) cation bridge. (Adapted from Franchi et al. (2003), Saeki and Sakai (2009) and Yu et al. (2013)).

Thus far, most studies on the adsorption of natural free DNA to soil have been based on adsorption experiments, i.e. the study of adsorption dynamics (Lajmi et al., 2020; Pang et al., 2022) or adsorption isotherms (Gardner and Gunsch, 2017; Hou et al., 2014) of DNA to different soil constituents, especially clay minerals (Saeki et al., 2011b). Many adsorption experiments have been conducted under different pH conditions (Saeki et al., 2010), which alter the charge of the DNA molecules and control the electrostatic forces (Sodnikar et al., 2021; Vandeventer et al., 2012). Adsorption experiments have also been conducted by adding ligands to compete for adsorption sites with the phosphate groups in DNA molecules, by for example, adding phosphate (Min et al., 2014) or sodium metaphosphate (SMP) (Cai et al., 2006) that contains free phosphate. And adsorption experiments have been conducted by adding different cations (e.g., Na^{+},Ca^{2+} or Fe^{3+}) to investigate the effect of cation bridges on retention

too (Sheng et al., 2019). However, these studies rarely explored the role of the four mechanisms simultaneously on free DNA transport through real soil.

Recently, degradation experiments, adsorption experiments and sand column experiments have been conducted to explore the degradation and adsorption mechanisms of free synthetic DNA tracers to porous media (Mikutis et al., 2019; Pang et al., 2022; Zhang et al., 2021). Using flanking regions on each end of DNA tracer could protect the internal amplicon that was analyzed with qPCR (Pang et al., 2022). However, adding flanking regions means the total length of the DNA tracer molecule is increasing and a longer total length means more sites are available for adsorption when transporting through porous media as demonstrated by Zhang et al. (2021).

Therefore, the objectives of this study are 1) to reveal the adsorption mechanisms of free DNA through real soil under flood irrigation conditions, and 2) to reveal the relative importance of the main adsorption mechanisms, i.e., what roles do the electrostatic forces, Van der Waals interactions (mainly hydrogen bond), ligand exchange, and/or cation bridge play?

2. Materials and Methods

2.1 The free DNA tracer

For this study an 88 nucleotides (nt) T12 ssDNA sequence was adopted from (Wang et al., 2022), whose uniqueness was confirmed using the Basic Local Alignment Search Tool (BLAST) and by comparing the sequence against the National Center for Biotechnology Information (NCBI) database (https://www.ncbi.nlm.nih.gov/) to ensure that the primers do not target any documented environmental DNA sequences (e.g., genomic DNA of microorganisms). The HPLC purified T12 ssDNA sequence

was ordered from the Sangon Biotech (Shanghai) Co., Ltd. as lyophilized ssDNA and was frozen at −20°C until use.

Table 1. The sequence of the synthetic DNA tracer.

	DNA sequence
T12	5'- C**CG TAG AGA TCT CCC ATC TGT CCT TTG** CTG AAG GTT AAA ACC CCG GAC CGC CTA GAA TAT TC*T TTC TTT AGC TCC AAA ATG GCC TCT* C -3'

Bold and underlined: forward primer

Italic and underlined: reverse primer

The concentration of the T12 ssDNA in the samples was measured using quantitative real-time polymerase chain reaction (qPCR) following the same procedure provided by (Wang et al., 2022). Samples were prepared for a 96-well plate by mixing 6 µl of each collected sample, with 10 µl of the SsoAdvanced™ Universal SYBR® Green Supermix, 0.5 µL of each forward and reverse primer, and 3 µL of nuclease-free water prior to analysis with a Bio-Rad CFX96 Touch (Hercules, CA, USA). Triplicates of each sample as well as triplicates of negative controls and 7 standards (i.e., samples of known concentrations ranging from 100 – 10^8 copies) were included on each plate and a standard curve was produced to relate the quantification cycle (Cq) value to DNA copy count. The DNA copy counts were measured based on a sample volume of 6 µL and then converted to concentrations in copies/ml.

2.2 The soil

Topsoil (0-20 cm) was excavated from a watermelon field near Yulongsha Lake (119.02°E, 42.94°N) in Chifeng City, Inner Mongolia and air-dried. To minimize

physical filtration, mainly straining, the soil was passed through a 50 μm pore size sieve (100 g soil were sieved for 20 min at a time through a 50 μm sieve) after thorough mixing to remove most of the silt and clay particles, although there were still some fine silt and clay particles attached to sand particles. The resulting soil was of a sandy soil texture with 92.23 % sand (>50 μm), 5.81 % silt (2-50 μm) and 1.96 % clay (<2 μm) by volume (Figure 1a), measured by a Mastersizer 2000 (Malvern, UK). The electrical conductivity, pH and cation exchange capacity (CEC) of the soil are 7.85 μS/cm, 7.35 and 2.64 meq/100 g, respectively, in the range of a typical sandy soil in North China. The mineral composition of the soil are shown in Table S1.

Given the differential particle size distribution by volume (Figure 1a), we calculated the specific surface area per unit volume of the soil. Specifically, assuming that the sand and silt particles ≥ 2 μm are spherical, we could obtain the specific surface area per unit volume (A/V) using Eq. (1) and then converted the differential particle size distribution by volume to the differential particle size distribution by surface area for the sand and silt portion.

For a spherical particle of diameter *D*, its volume (*V*) and surface area (*A*) can be calculated by:

$$\mathrm{V} = \frac{4}{3}\pi\left(\frac{D}{2}\right)^3, \mathrm{A} = \pi D^2 \quad (1)$$

Then the specific surface area per unit volume (*A*/*V*) would be:

$$\frac{A}{V} = \frac{6\pi D^2}{\pi D^3} = \frac{6}{D} \quad (2)$$

Whereas, for the clay particles < 2 μm, assuming that the clay particles are illite which take up 93% of clay minerals (Table S1), we use the typical specific density (2.6 g/cm^3) and specific surface area (80-150 m^2/g) of illite (McBride, 1994) to calculate the differential particle size distribution by surface area for the clay texture portion.

Specifically, for each clay particle size *d*, the differential particle size distribution by volume was multiplied by the specific density (2.6 g/cm^3) and the specific surface area (using the lower limit of 80 m^2/g to be conservative) to obtain the differential particle size distribution by surface area. Then, combining the differential particle size distribution by surface area for sand and silt portion and for clay portion, the differential and cumulative particle size distribution by surface area of the soil was obtained, as shown in Figure 1b. It can be seen that although clay (<2 μm) only took up 1.96 % by volume (Figure 1a), it took up over 97.70 % by surface area (Figure 1b).

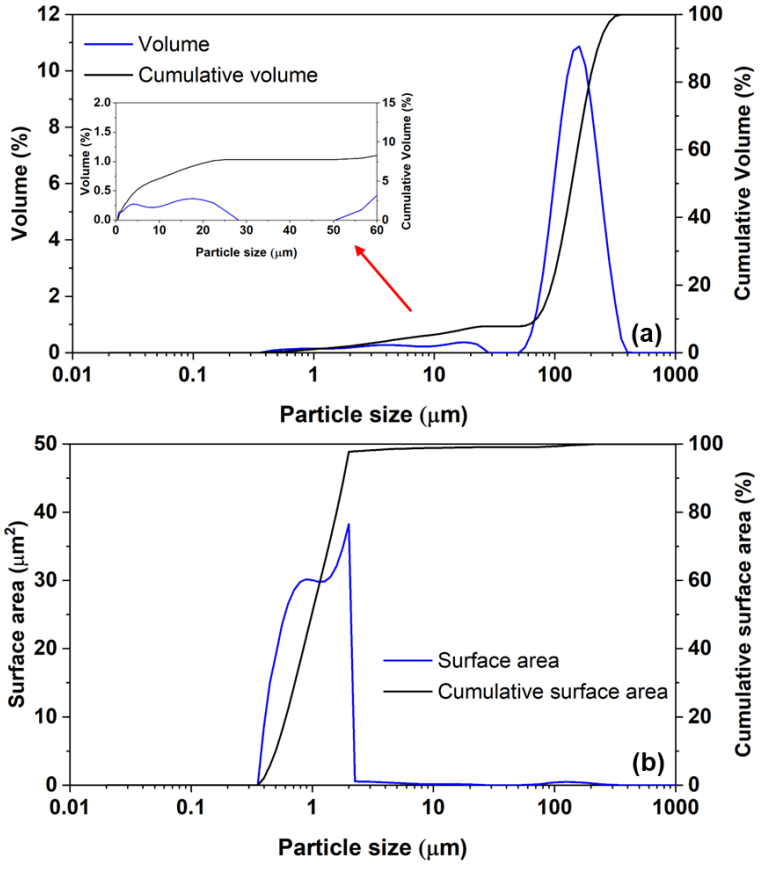

Figure 1. The differential and cumulative soil particle size distribution by volume (a) and by surface area calculated assuming soil particles are spheres (b).

175 *2.3 Soil column experiments*

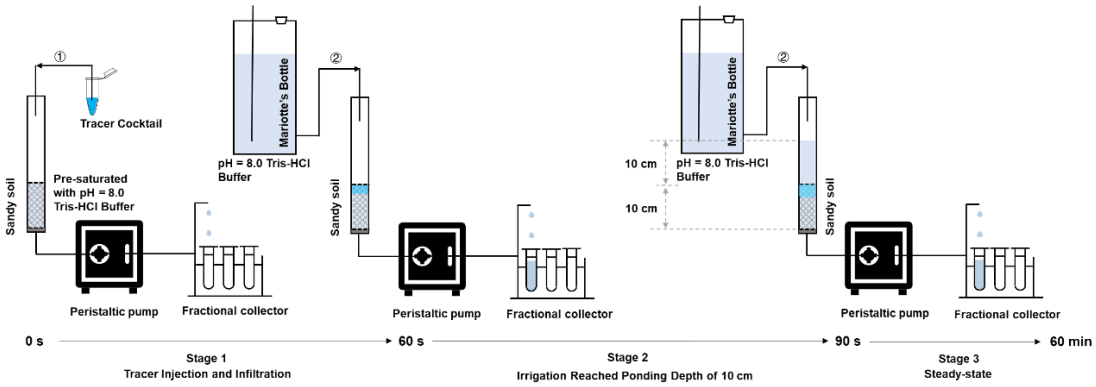

176

177 **Figure 2.** The soil column experimental setup.

178

179 A total of 15 transparent polyvinylchloride (PVC) columns (30 cm long, 3 cm inner
180 diameter) were packed with 10 cm of the sandy soil to test DNA tracer transport through
181 real soil. The 10 cm sandy soil (as described at Section 2.2) was screened with a
182 perforated plastic plate (diameter of 3 cm, pore size of 0.2 cm) on the top to avoid
183 disturbance of the soil surface by the influent tracer or irrigation water. The bottom of
184 the column was screened with a perforated plastic plate (diameter of 3 cm, pore size of
185 0.2 cm) that was covered by filter paper (diameter of 3 cm, pore size of 7-8 μm) to
186 avoid soil leakage. All of the soil columns were packed to a bulk density of ρ_b = 1.51
187 g/cm^3, and pre-saturated from bottom for 8 hr with a 0.01 mol/L (Exp 1) or 0.05 mol/L
188 (Exp 2-5) pH=8.0 Tris-HCl buffer (Table 2). This was done to ensure full saturation
189 (saturated water content θ_s = 0.44 cm^3/cm^3 and pore volume (PV) = 31.5 cm^3) and to
190 reach an initial pH=8.0 over the entire soil column in order to exclude the effect of pH
191 on electrostatic forces.
192 Each experimental run was conducted in three stages under saturated conditions. First,
193 the pre-saturated soil column was set vertically and was immediately connected to a
194 peristaltic pump and then to a fractional collector (Figure 2). In stage 1, 5 ml (0.167

pore volume) of a tracer solution (adjusted to pH=8.0 by adding 5 mol/L NaOH right before injection) was pulse injected over 2 s at the top of the column (Figure 2①). The solution took about 60 s to fully infiltrate into the soil with the help of the peristaltic pump (Figure 2 Stage 1).

Table 2. The compositions of the 5 different tracer solutions and the experimental condition during the 5 different experiments.

		Unit	Exp 1	Exp 2	Exp 3	Exp 4	Exp 5
Tracer solution	T12 DNA	copies/ml	3E+14	3E+14	3E+14	3E+14	3E+14
	KBr	mmol/l	10	10	10	10	10
	Tris	mol/l	0.01	0.1	0.1	0.1	0.1
	EDTA	mol/l	0.001	0.1	0.1	0.1	0.1
	Na_2HPO_4	mol/l	0	0	0.1	0.5	0
	$(NaPO_3)_6$	mol/l	0	0	0	0	0.1
	pH		8.0	8.0	8.0	8.0	8.0
Tris-HCl buffer	Tris	mol/l	0.01	0.05	0.05	0.05	0.05
	pH		8.0	8.0	8.0	8.0	8.0
	Temperature	℃	22 ± 1	22 ± 1	22 ± 1	22 ± 1	22 ± 1

As shown in Table 2, the constituents of the tracer solutions were different in the five triplicated experiments. In Exp 1, a baseline solution was used consisting of 3E+14 copies/ml of the T12 ssDNA tracer, 0.01 mol/L Tris, and 0.001 mol/L EDTA imitating the pH=8.0 TE buffer which is a typical DNA storage solution (Nguyen and Elimelech, 2007; Sambrook et al., 1989), and 10 mmol/L KBr as a reference tracer. For Exp 2 to Exp 5, the 3×10^{14} copies/ml T12 ssDNA tracer and the 10 mmol/L KBr were maintained, but the concentrations of Tris and EDTA were raised to 0.1 mol/L to better buffer the pH and fully chelate the multivalent cations. In Exp 3, 0.1 mol/L Na_2HPO_4 was added as competing ligand to compete adsorption sites with the phosphate groups in DNA molecules and investigate the role of ligand exchange. In Exp 4, the concentration of

213 Na_2HPO_4 was raised to 0.5 mol/L to occupy more adsorption sites. Finally, in Exp 5,
214 0.1 mol/L $(NaPO_3)_6$ was added as a stronger competing ligand, as 0.1 mol/L $(NaPO_3)_6$
215 could theoretically provide 0.6 mol/L PO_3^-. The Tris, EDTA, Na_2HPO_4, $(NaPO_3)_6$ and
216 KBr were purchased from Shanghai Macklin Biochemical Technology Co., Ltd.
217 Stage 2 started when the tracer solution just fully infiltrated into the soil (Figure 2 Stage
218 2). A Mariotte's bottle was used to pond the sandy soil with 0.01 mol/L (Exp 1) or 0.05
219 mol/L (Exp 2-5) of pH=8.0 Tris-HCl buffer (Figure 2②), until a 10 cm water head was
220 reached (taking about 30 s), mimicking flood irrigation.
221 Stage 3 started when the ponded water reached 10 cm. The Mariotte's bottle was used
222 to continuously supply the 0.01 mol/L (Exp 1) or 0.05 mol/L (Exp 2-5) pH=8.0 Tris-
223 HCl buffer (Figure 2②) and maintain the 10 cm ponded water throughout the
224 experiment, to reach a constant flow of 5 ml/min with the help of the peristaltic pump
225 until the end of the 1-hr experiment (Figure 2 Stage 3).
226 The laboratory temperature was controlled by air conditioner at 22 ± 1 □ to exclude the
227 effect of temperature on the adsorption mechanisms, as adsorption releases heat (Mason
228 et al., 2015). Each sample collected by the fractional collector was weighed, and then a
229 100 μl subsample was saved and frozen at -20 °C until DNA tracer analysis via qPCR.
230 The rest of the sample was stored at 4 °C until Br analysis with an ion selective electrode
231 (ISE, D10-35, Orion Dual Star, US) after dilution. The Br concentration in each sample
232 was then scaled by the dilution factors.
233 *2.4 Water flow and reference tracer Br transport modeling*
234 Although the water flow was set to be constant (5 ml/min), the best fit saturated
235 hydraulic conductivity (K_s, cm/min) of each experiment (Tables 3 and S3) was inversely
236 solved by fitting the Richard's equation to the measured discharge obtained by
237 weighing each sample. The residual water content, the inverse of the air-entry value,

and the pore-size distribution index was ineffective under fully saturated condition (Table S3).

Based on the well simulated water flow (Figure S1) and the obtained soil hydraulic parameters (θ_s and K_s), the longitudinal dispersivity (D_L, cm) was inversely solved by fitting the advection-dispersion equation (Zhao et al., 2022) to the measured Br breakthrough curve:

$$\frac{\partial \theta_s C_{Br}}{\partial t} = \theta_s D_{Br}^{w} \frac{\partial^2 C_{Br}}{\partial x^2} - q \frac{\partial C_{Br}}{\partial x} \quad (3)$$

$$\theta_s D_{Br}^{w} = D_L K_s + \theta_s^{4/3} D_{w\_Br} \quad (4)$$

where, C_{Br} is the bromide concentration in soil water (mmol/ml), t is the time (min), x is the vertical transport distance along the soil column (cm), D^w_{Br} is the dispersion coefficient tensor for Br (cm^2/min), q is the volumetric flux density (cm/min), D_{w_Br} (=1.89E-03 cm^2/min) is the molecular diffusion coefficient of Br in free water (Yaws, 2009).

2.5 DNA tracer fate and transport modeling

Wang et al. (2022) recently proved that the two-site kinetic sorption model developed by Schijven and Simunek (2002) implemented in HYDRUS (Šimůnek et al., 2008) could well capture the transport of free DNA tracer through loamy sand textured porous media. Thus, based on the well simulated water flow and reference tracer Br, the two-site kinetic sorption model in HYDRUS-1D is adopted here to simulate the fate and transport of the T12 DNA tracer through the saturated soil column:

$$\frac{\partial C}{\partial t} + \frac{\rho_b}{\theta_s}\left(\frac{\partial S_1}{\partial t} + \frac{\partial S_2}{\partial t}\right) = D^w \frac{\partial^2 C}{\partial x^2} - V \frac{\partial C}{\partial x} - \mu_w \theta_s C - \mu_s \rho_b (S_1 + S_2) \quad (5)$$

$$\rho_b \frac{\partial S_1}{\partial t} = \theta_s k_{a1} C - k_{d1} \rho_b S_1 - \mu_s \rho_b S_1 \quad (6)$$

$$\rho_b \frac{\partial S_2}{\partial t} = \theta_s k_{a2} C - k_{d2} \rho_b S_2 - \mu_s \rho_b S_2 \quad (7)$$

261 $$\theta_s D^w = D_L K_s + \theta_s^{4/3} D_w \quad (8)$$

262 where, C is the DNA concentration in the aqueous phase (copies/ml), S is the DNA
263 concentration (copies/g) on kinetic sites (e.g. attached DNA molecules), given the
264 saturated condition of our study, porosity θ_s (m^3/m^3) is used to substitute the water
265 content θ in Eqs. 5-8, ρ_b is the dry bulk density (kg/m^3), D^w is the dispersion coefficient
266 tensor of DNA (cm^2/min), $V=U/\theta_s$ is the pore-water velocity (cm/min), D_L is the
267 longitudinal dispersivity (cm) inherited from the Br tracer, D_w is the molecular diffusion
268 coefficient of DNA in free water, 2.655E-06 cm^2/min (Robertson et al., 2006). The first-
269 order degradation rate constants of the DNA in water (μ_w) and attached to soil (μ_s) were
270 found by trial and error. And the attachment and detachment rates of the two kinetic
271 sorption sites (k_{a1}, k_{a2}, k_{d1} and k_{d2}) were obtained by fitting the model to the measured
272 DNA tracer breakthrough curve.
273
274 *2.6 The domain setup and initial and boundary conditions*
275 The 10 cm soil profile was divided into 0.1 cm intervals and one observation node was
276 set at the lower boundary (Figure S1a). The total simulation time was 60 min, and the
277 initial time step, the minimum time step and maximum time step were set to 0.01 min,
278 0.00144 min and 1 min, respectively.
279 Corresponding to the three stages of each experimental run (Figure 2), the numerical
280 simulation was also divided into three stages. In Stage 1, 0-60 s, the DNA tracer solution
281 was injected in t=0-2 s with a maximum ponded water of 0.7 cm (corresponding to the
282 5 ml tracer solution) until it fully infiltrated into the soil profile (Figure 2 Stage 1). In
283 this stage, the pressure head profile was changing and unknown. Thus, the water flow
284 was simulated to obtain the pressure head profile of the whole system from the moment
285 when the DNA tracer solution was applied until the moment when it just fully infiltrated

into the soil, i.e., pressure head at the upper boundary is 0. Specifically, the upper boundary condition was set to be an atmospheric BC with surface layer ≤ 0.7 cm and the lower boundary condition was set to be a constant pressure head of 0 (Figure S1a). The atmospheric BC was set to be precipitation for 0-2 s to reflect the injection of the tracer solution at a rate of 0.35 cm/s at the beginning of the experiment and then the precipitation was set to zero for 2-60 s to describe the infiltration into the soil profile. The water flow simulation of this stage provided the variable pressure head at the upper boundary during 0-60 s (Figure S2a).

In Stage 2, 60-90 s, flood irrigation was added until 10 cm of ponded water was reached (Figure 2 Stage 2). In this stage, the pressure head profile was also changing and unknown. Thus, the water flow was simulated to obtain the pressure head profile of the whole system from the moment when the irrigation and ponding started until the moment when the ponded water reached a head of 10 cm. The initial pressure head of the whole system during this stage was inherited from the last moment of the 0-60 s (Stage 1) simulation. The upper boundary condition was set to be an atmospheric BC with surface layer ≤ 10 cm and the lower boundary condition was kept at a constant pressure head of zero (Figure S1b). The atmospheric BC was set to be precipitation for the times 60-90 s of the experiment at a precipitation rate of 0.36 cm/s, to describe the experimental condition that in 60-90 s flood irrigation was imposed and reached a ponding water depth of 10 cm. The water flow simulation of this stage provide the variable pressure head at the upper boundary during 60-90 s (Figure S2b).

In Stage 3, 90 s-60 min, the system was maintained at steady-state (Figure 2 Stage 3), a pressure head at the upper boundary of 10 cm was maintained, and the lower boundary condition was free drainage. Thus, combining the three stages together, the upper

boundary condition was set to a variable pressure head, which was obtained by the simulation results of Stages 1 and 2 during 0-90 s and kept constant at 10 cm during 90 s-60 min (Figure S2c), and the lower boundary condition was free drainage throughout the simulation (Figure S1c). For both the Br and DNA transport simulations, the upper boundary was set to be a concentration flux while the bottom boundary was set to a zero concentration gradient (Figure S1d). During 0-60 s during when the tracer solution was injected and infiltrated into the soil, the concentration of Br and DNA in the incoming water at the upper boundary was set to be the concentration of KBr and T12 DNA in the tracer solution as listed in Table 2, respectively. While from 60 s-60 min, the concentration of Br and DNA in the incoming water at the upper boundary was set to zero.

3. Results and discussion

3.1 Breakthrough curve and retention profile of DNA tracer

The cumulative discharge (R^2=0.999 and NSE=0.999) of the 5 triplicated soil column experiments were captured very well by the Richard's equation (Figure S3). The inversely solved best fit saturated hydraulic conductivity (K_s) of the 5 triplicated experiments was 0.70±0.02 cm/min (Table 4). The Br peaked at 7 min in all five experiments, with a recovery rate of 97 % ±6 % (Table 3) and the breakthrough curves of Br were well captured by the advection-dispersion equation with R^2=0.91-0.98 and NSE=0.83-0.92 (Figure 3). Based on the well-captured water flow and Br breakthrough, DNA tracer breakthrough curves were well captured too by the two-site kinetic sorption model with R^2= 0.83-0.91 and NSE=0.79-0.89 (Figure 3). The R^2 and NSE of the two-site kinetic sorption model simulating DNA tracer could not compete with R^2 and NSE

of the advection-dispersion equation simulating Br, because the way the DNA concentration was measured caused the data to scatter (Wang et al., 2022). Specifically, each discharge sample was diluted by a factor of 1000, and then a 6 µl subsample was taken from the 1000-fold diluted sample for DNA copy analysis. The measured DNA copies were multiplied by 1000×1000/6 = 1.7E+05 to obtained the original concentration (copies/ml) of the sample. This means that any small error in diluting the sample, taking the subsample, or during the qPCR analysis would be amplified by a factor of 1.7E+05 in the measured DNA concentration.

Then, the two-site kinetic sorption model validated by the DNA tracer breakthrough curves was used to reveal the dynamics of DNA tracer in the soil profile (Figure 4).

In Exp 1, the T12 DNA tracer was dissolved in a standard pH=8.0 TE buffer commonly used for storing DNA (Nguyen and Elimelech, 2007; Sambrook et al., 1989) that was injected into the soil together with a reference Br tracer, after which the field was flood irrigated. The recovery rate of the free DNA tracer during the 1-hr experimental period was only 4.9 % (Table 3).

Before exploring the adsorption/desorption rates and mechanisms, we need to exclude the mass loss due to degradation from the total amount that did not pass through (1 - 4.9 % = 95.1 %). As described in section 2.2, the soil was excavated from a watermelon field, therefore the degradation rate of the free DNA tracer in soil pore water (μ_w) was adopted from the degradation rate of extracellular DNA (eDNA) in agriculture soil measured by Sirois and Buckley (2019). Specifically, assuming first-order degradation, the degradation rate (μ_w) can be obtained from the data they provided as remaining 0.05 % eDNA after 7 days via μ_w = -ln(0.05 %)/7/24/60 = 5.3E-04 min^{-1}. This degradation rate was equivalent to a mass loss of 3.1 % free DNA tracer in our 1-hr experiment. Wang et al. (2022) proved that the degradation of the DNA tracer was inhibited once the DNA

attached to the porous media at which point the model was insensitive to the degradation rate of the DNA tracer mass fraction that attached to soil (μ_s) as long as it was one magnitude lower than μ_w. Thus, we set the μ_w to 5.3E-05 min^{-1}, one magnitude lower than μ_w. As a result, the DNA tracer retention mechanisms in the experimental soil should explain the rest 1 - 4.9 % - 3.1 % = 92 % of injected mass.

The peak time of the breakthrough curve (11 min) was delayed by 4 min compared to that of Br, and DNA tracer breakthrough curves generally had thicker tails than the Br tracer (Figure 3a). When the DNA tracer fully infiltrated into the soil, the liquid-phase DNA tracer concentration in the profile (Figure $4a_1$ shadow region) peaked at 0.2 cm at 1 min, after which the peak of the liquid-phase DNA tracer concentration kept moving downward in the profile indicating the movement of the center of mass of the dissolved DNA tracer. The liquid-phase DNA tracer concentration peaked at 0.8 cm at 1.5 min when the 10 cm pressure head was reached at the surface of the column. The liquid-phase DNA tracer concentration peaked at 11 min at the bottom of the soil column (10 cm depth) synchronous to the time when the DNA concentration peaked in discharge (Figure $4a_1$). Overall, the attachment of DNA to kinetic site 1 (Figure $4b_1$) followed the trend of the movement of the liquid-phase DNA tracer but was retarded (Figure $4a_1$). The DNA attachment to the kinetic sorption site 1 peaked at 0.1 cm at 1 min (Figure $4b_1$), retarded by 0.1 cm compared to the liquid-phase DNA tracer concentration (Figure $4a_1$). And the peak of the DNA attachment to the kinetic sorption site 1 kept moving downward (Figure $4b_1$), peaking at 0.7 cm at 1.5 min when the 10 cm pressure head was fully established atop of the column. And then the DNA attachment to the kinetic sorption site 1 peaked at 1.2 cm at 2 min (Figure $4b_1$, caught up with the peak of liquid-phase DNA tracer concentration in the profile (Figure $4a_1$)), and finally peaked at 11 min at the bottom of the soil column (10 cm depth, Figure $4b_1$)

when the DNA concentration peaked in the discharge (Figure 3a). The decreased adsorption from 60 s to 60 min (Figure 4b$_1$) and the comparable attachment rate (k_{a1} = 13.8 min^{-1}) and detachment rate (k_{d1} = 14.7 min^{-1}) (Table 4) indicated that the kinetic sorption site 1 was a reversible adsorption site.

In contrast, the kinetic sorption site 2 was almost irreversible (k_{a2} = 0.687 min^{-1}, k_{d2} = 7E-03 min^{-1}), as the attachment kept increasing after tracer injection, before a gradual decrease was observed after the peak concentration was reached at 15 min (4 min after the concentration peak of DNA tracer in discharge). Also, except for the first stage (0-1 min), the attachment to the kinetic sorption site 2 was one to three orders of magnitude higher than the attachment to the kinetic sorption site 1 (comparing Figure 4c$_2$-c$_5$ with Figure 4b$_2$-b$_5$). Therefore, the retention of the DNA was dominated by the almost irreversible kinetic sorption site 2.

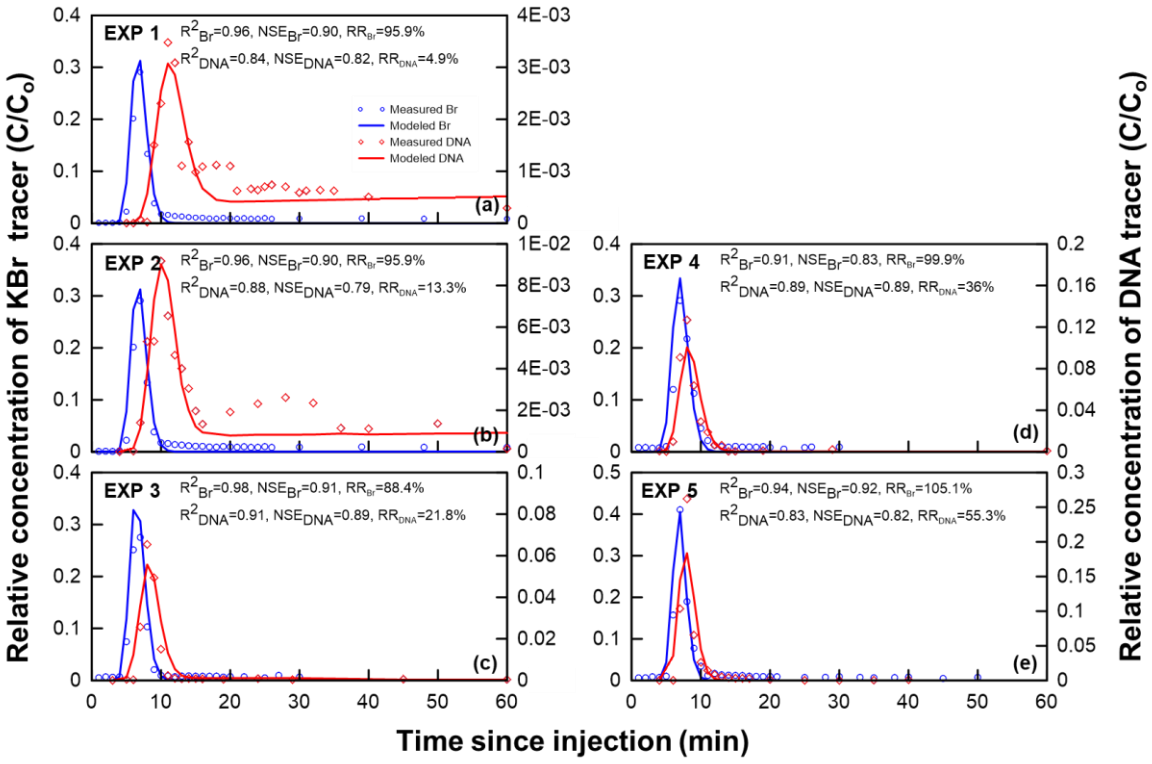

Figure 3. Observed and HYDRUS-1D simulated relative concentration of the reference tracer Br (in blue) and DNA tracer (in red) from the 5 triplicated experiments. The dots

399 demonstrate the average of the triplicated experiments, while the lines demonstrate the
400 model simulation.
401
402 **Table 3.** The peak time (min), relative peak concentration (C_{max}/C_o) and tracer mass
403 recovery (%) in each triplicated experiment.

Experiment	Tracer	Peak time (min)	Peak concentration (C_{max}/C_o)	Mass recovery (%)
Exp 1	Br	7	0.29±0.04	96±8.5
	DNA	11	0.0035±0.0013	4.9±1.6
Exp 2	Br	7	0.29±0.04	96±8.5
	DNA	10	0.0092±0.0045	13.3±2.3
Exp 3	Br	7	0.28±0.08	88±4.1
	DNA	8	0.066±0.013	21.8±0.5
Exp 4	Br	7	0.29±0.022	100±8.1
	DNA	8	0.13±0.024	36.0±2.3
Exp 5	Br	7	0.41±0.044	105±1.1
	DNA	8	0.26±0.068	55.3±2.9

404
405 **Table 4.** Water flow, reference tracer Br and DNA tracer transport simulation
406 parameters.

	Tracers	K_s (cm/min)[a]	D_L (cm)[b]	k_{a2} (min^{-1})[c]	k_{d2} (min^{-1})[c]	k_{a1} (min^{-1})[c]	k_{d1} (min^{-1})[c]	R^2	NSE
Exp 1	Br	0.68	0.149	-	-	-	-	0.96	0.90
	DNA	0.68	0.149	0.687	7E-03	13.8	14.7	0.84	0.82
Exp 2	Br	0.68	0.149	-	-	-	-	0.96	0.90
	DNA	0.68	0.149	0.533	7E-03	10.9	15.4	0.88	0.79
Exp 3	Br	0.71	0.149	-	-	-	-	0.98	0.91
	DNA	0.71	0.149	0.288	3.4E-03	6.83	18.28	0.91	0.89
Exp 4	Br	0.69	0.149	-	-	-	-	0.91	0.83
	DNA	0.69	0.149	0.147	1.2E-03	5.53	22.47	0.89	0.89
Exp 5	Br	0.71	0.11	-	-	-	-	0.94	0.92
	DNA	0.71	0.11	0.095	9E-04	4.88	25.39	0.83	0.82

407 K_s is the saturated hydraulic conductivity, D_L is the longitudinal dispersivity, k_a and k_d

are attachment and detachment rate coefficients, respectively, and subscripts 1 and 2 referring to the two kinetic sorption sites.

[a]Parameter is inversely solved by fitting to measured discharge.

[b] Parameter is inversely solved by fitting to measured reference tracer Br breakthrough curve.

[c] Parameters inversely solved by fitting to measured DNA tracer breakthrough curve.

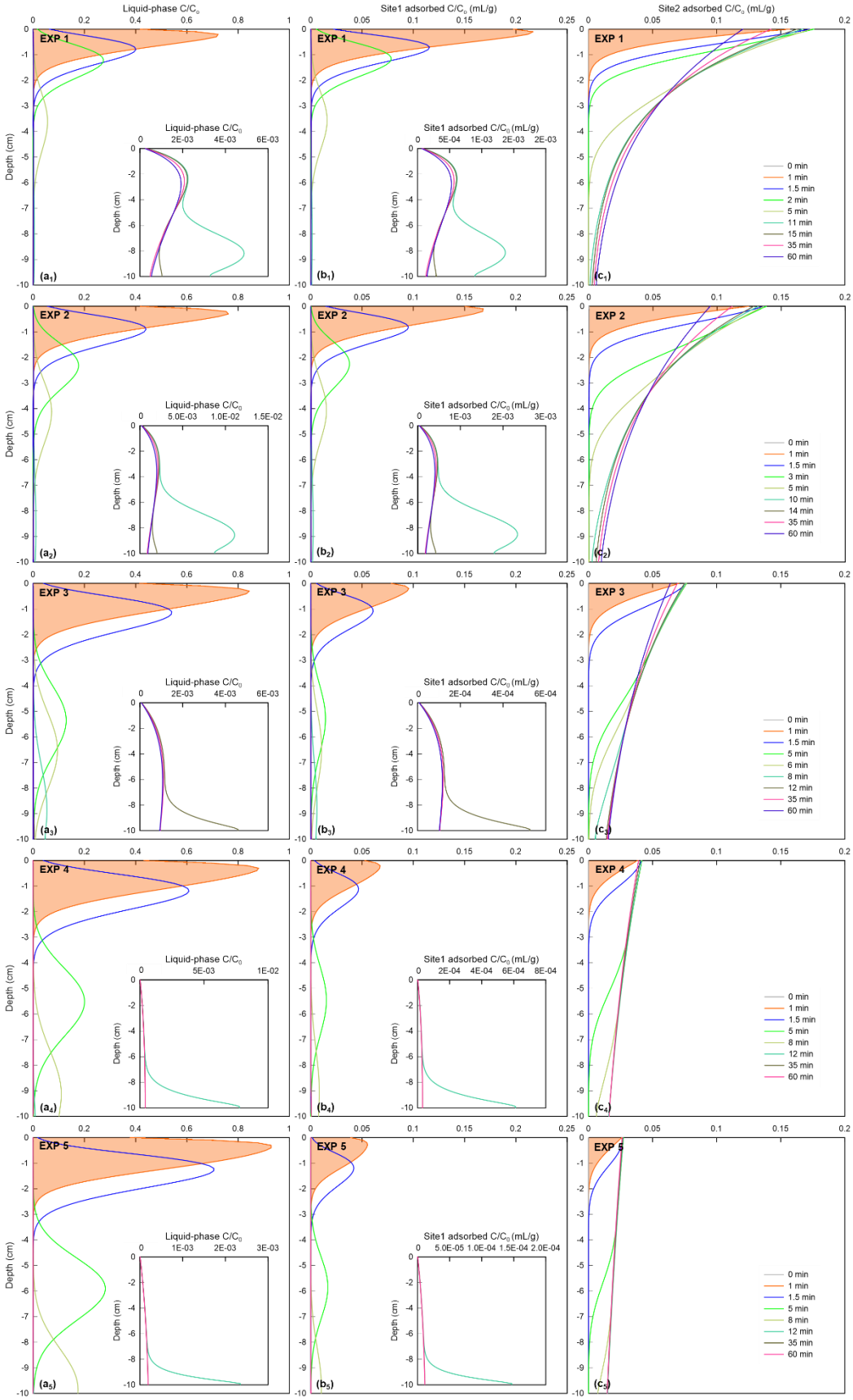

415

416 **Figure 4.** Simulated dynamics of the DNA tracer in the soil profile of Exp 1-5. The left

column is the relative concentration of DNA in liquid-phase (C/C_o), the middle column is the relative concentration of DNA adsorbed to the kinetic sorption site 1 (adsorbed C/C_o), and the right column is the relative concentration of DNA adsorbed to the kinetic sorption site 2 (adsorbed C/C_o). The inset plots demonstrate the very low C/C_o values which would be hard to see in the soil profile plots.

3.2 The role of cation bridges

In Exp 2 all the condition were kept the same as in Exp 1, but 1) the concentration of Tris was increased in the tracer solution from 0.01 M to 0.1 M and the concentration of Tris in the Tris buffer was increased from 0.01 M to 0.05M (which is the standard concentration of the Tris-HCl buffer), and 2) the concentration of EDTA in the tracer solution was increased from 0.001 M to 0.1 M (Table 2). Increasing the concentration of Tris was to maintain the pH stable at 8.0. While increasing the concentration of EDTA was to fully chelate the multivalent cations and reveal the role of cation bridging. The peak time of DNA in Exp 2 was 1 min ahead of that of Exp1, the relative peak concentration of DNA (C_{max}/C_o) was increased 2.6-fold, and the DNA mass recovery was increased 2.7-fold (Figures 2a and 2b and Table 3). In comparison to Exp 1, the liquid-phase DNA tracer concentration increased by 16 % (Figures $4a_1$ and $4a_2$ shadow area) when the DNA tracer fully entered the soil at 1 min. Meanwhile, the attachment to the kinetic sorption site 1 and 2 decreased by 13 % (Figure $4b_1$ and $4b_2$ shadow area) and 12 % (Figure $4c_1$ and $4c_2$ shadow area), respectively. And k_{d1}/k_{a1} was increased from 1 (Exp 1) to 1.5 (Exp 2) and k_{a2} decreased from 0.687 min^{-1} (Exp 1) to 0.533 min^{-1} (Exp 2). These can be explained by the two roles of EDTA: its ability to inhibit adsorption by breaking down cation bridges and inhibiting degradation by hiding the Mg^{2+} from Dnase I. The multivalent cations that could potentially form cation bridges between the

442 negatively charged DNA and the negatively charged tetrahedral silica layer on the clay
443 surface was chelated by EDTA, resulting in inhibited adsorption of DNA. Also, EDTA
444 chelated the Mg^{2+} which is required for the DNase I to decay DNA, and inhibited
445 degradation (Liang and Keeley, 2013). Thus, the mass recovery increased from the
446 baseline 4.9 % in Exp 1 to 13.3 % in Exp 2 due to the inhibited mass loss (due to
447 degradation, estimated to be 3.1 %) and the inhibited adsorption by cation bridges (13.3 %
448 - 4.9 % - 3.1 % = 5.3 %). The degradation of the free DNA tracer in Exp 2-Exp 5 was
449 inhibited by the high concentration of EDTA in the tracer solution.
450
451 *3.3 The role of ligand exchange*
452 In Exp 3 all conditions were kept the same as in Exp 2, except 0.1 M of Na_2HPO_4 was
453 included in the tracer solution. Compared to Exp 2, the liquid-phase DNA tracer
454 concentration increased by 35 % after the tracer had fully entered the soil after 1 min
455 (Figure 4a_2-a_3 shadow region), and the attachment to the kinetic sorption site 1 and 2
456 decreased by 29 % (Figure 4b_2-b_3 shadow region) and 30 % (Figure 4c_2-c_3 shadow
457 region), respectively. The peak concentration of DNA increased 8-fold, and the mass
458 recovery of DNA doubled (from 13.3 % to 21.8 %) (Figure 3c). The free phosphate
459 provided by the Na_2HPO_4 is 6 orders of magnitude greater than the phosphate groups
460 that occur in the 88 nt ssDNA tracer molecules (Table S2). Thus, the free phosphate in
461 the injection solution competed with the phosphate groups of the DNA tracer and
462 occupied the adsorption sites on the edges of clay minerals, inhibiting the adsorption of
463 DNA, which is consistent with the finding of Saeki et al. (2010). The inversely solved
464 k_{a1}, k_{a2} and k_{d1} captured well the peak timing and C_{max}, the k_{d1} (18.28 min^{-1})/k_{a1} (6.83
465 min^{-1}) of Exp 3 was about 3, and k_{a2} was significantly decreased from 0.533 min^{-1} (Exp
466 2) to 0.288 min^{-1} (Exp 3). While k_{d2} captured well the tailing part, which decreased

467 from 7E-03 min^{-1} (Exp 2) to 3.4E-03 min^{-1} (Exp 3).

468 In Exp 4 the concentration of Na_2HPO_4 was further increased to 0.5 M. Consequently,
469 the liquid-phase DNA tracer concentration further increased by 7 % at 1 min (Figures
470 $4a_3$ and $4a_4$ shadow region), and the DNA attachment to the kinetic sorption site 1 and
471 2 further decreased by 26 % (Figures $4b_3$ and b_4 shadow region) and 44 % (Figures $4c_3$
472 and $4c_4$ shadow region), respectively. As a result, the peak concentration of DNA
473 doubled and mass recovery increased further from 21.8 % to 36.0 %, but the marginal
474 effect of adsorption site occupation decreased. This means that there must be a limit to
475 the ability of the Na_2HPO_4 phosphate to block attachment sites for the DNA. The k_{d1}
476 (22.47 min^{-1})/k_{a1} (5.53 min^{-1}) continued to increase to 4, and k_{a2} decreased from 0.288
477 min^{-1} (Exp 3) to 0.147 min^{-1} (Exp 4), as more phosphate occupied the adsorption and
478 inhibited DNA adsorption. Note that the θ_s becomes 0.46 due to some dispersion of soil
479 particles.

480 Similarly, in Exp 5 the 0.5 M of Na_2HPO_4 was replaced by 0.1 M $(NaPO_3)_6$, which
481 increased the DNA recovery rate from 36.0 % (Figure 3e) to 55.3 % (Figure 3f), further
482 confirming the effect of adsorption site occupation and competition, as 0.1 M $(NaPO_3)_6$
483 could ideally provide 0.6 M phosphate. The DNA attachment to the two kinetic sorption
484 sites was even less than observed in Exp 4. The attachment to the kinetic sorption site
485 1 and 2 decreased by 15 % (Figures $4b_4$ and $4b_5$ shadow area) and 30% (Figures $4c_3$
486 and $4c_4$ shadow area), respectively. And the detachment rate of DNA from the
487 reversible sites was increased from 22.47 min^{-1} to 25.39 min^{-1}, the k_{d1} (25.39 min^{-1})/k_{a1}
488 (4.88 min^{-1}) continued to increase to 5 and the attachment rate to the irreversible
489 sorption site decreased from 0.147 min^{-1} to 0.095 min^{-1}, which further confirmed the
490 effect of adsorption site occupation and competition. Admittedly, the initial
491 concentration of Exp 3-5 is more than that of Exp 2 (Table 2), but the phosphate groups

492 increased by this initial concentration increase was 6 orders of magnitude less than the
493 free phosphate increased by adding Na_2HPO_4 or $(NaPO_3)_6$ (Table S2) and could be
494 safely neglected. In addition, $(NaPO_3)_6$ is a dispersant that can be destructive to soil.
495 We did see a small amount of soil particles being dispersed and break through the filter
496 paper, which was collected in the sampling tubes. This means that the 0.1 M $(NaPO_3)_6$
497 was more than enough to release the DNA retained by ligand exchange, which takes up
498 42.0 % of the total injected mass (subtracting the mass recovery of Exp 2 from that of
499 Exp 5).

500 *3.4 The role of other mechanisms*

501 The rest of the DNA that could not be released by the 0.1 M $(NaPO_3)_6$ (44.7 %,
502 subtracting the mass recovery of Exp 5 from the unity) is likely retained by other
503 possible retention/adsorption mechanisms, such as Van der Walls interactions (mainly
504 hydrogen bond), electrostatic forces, and straining. The pH of the experimental system
505 was controlled at 8.0 to exclude the effect of pH on electrostatic forces and to keep the
506 electrostatic force at the same level for all the experiments. The presence of layer
507 silicate clays, including illite and smectite in the experimental soil, likely caused the
508 chemisorption of both anions and cations (McBride, 1994), including the negatively
509 charged free DNA tracer. We also note that although the clay particles took up over
510 97.70 % by surface area, there were sand and silt particles present in the soil as well.
511 The mineral composition of the soil (Table S1) indicated that the sand and silt particles
512 contained Al_2O_3 and Fe_2O_3 which are positively charged and could adsorb the
513 negatively charged DNA tracer molecules according to the findings of Zhang et al.
514 (2021).

515

4. Conclusions

Although synthetic DNA tracers have unparalleled advantages in tracking the connectivity between multiple sources and multiple sinks at very low detection limit, the application of DNA tracers to real soil textured systems is still at the pioneer stage due to the large size of encapsulated DNA tracers, its fast degradation, and strong adsorption to solid interfaces. Until recently, Wang et al. (2022) proved using both experiments and model simulations that free DNA tracers are a valuable tracer that can be used to describe transport in packed real soil textured porous media. Based on the combination of experimental data and numerical modeling using a two-site kinetic sorption model we can make the following conclusions: 1) the adsorption of the synthetic unencapsulated free ssDNA tracer (88 nucleotides) was dominantly to clay particles in the real soil, which took up 1.96 % by volume, but took up much more than 97.70 % by surface area; and 2) at a pore water pH of 8.0, excluding the 4.9 % passing through and 3.1 % degradation amount, the main retention mechanisms in the experimental soil were ligand exchange (42.0 %), Van der Waals interactions (mainly hydrogen bonds) electrostatic forces and straining (together 44.7 %), and cation bridge (5.3 %). The adsorption mechanisms of a free DNA tracer in real soil revealed it could facilitate the application of free DNA to trace vadose zone water flow and solute/ contaminant transport under flood irrigation and other infiltration conditions. For future studies, it is recommended to differentiate between Van der Waals interactions (mainly hydrogen bonds), electrostatic forces and straining by considering surface roughness, particulate composition, and mineral composition of soil particles.

Supporting Information

Figure S1, Figure S2, Figure S3, Table S1, Table S2, Table S3

Notes

The authors declare no competing financial interest.

Acknowledgement

This work was primarily supported by the National Natural Science Foundation of China [grant numbers: 52130902, 51909264], the National Key Research and Development Program of China [grant number: 2021YFD1900603], a Heising–Simons Foundation [grant number: 2014-59] and the National Natural Science Foundation of China [grant number: 52279051]. This work was also supported by the China Agricultural University Undergraduate Research Program [grant numbers: URP20201091002, X2021100190697].

Author Contributions

The manuscript was written with contributions of all authors. All authors have given approval to the final version of the manuscript.

References

Bulushev, R.D., Steinbock, L.J., Khlybov, S., Steinbock, J.F., Keyser, U.F., Radenovic, A., 2014. Measurement of the Position-Dependent Electrophoretic Force on DNA in a Glass Nanocapillary. Nano Letters, 14(11): 6606-6613. DOI:10.1021/nl503272r

Cai, P., Huang, Q., Zhang, X., Chen, H., 2006. Adsorption of DNA on clay minerals and various colloidal particles from an Alfisol. Soil Biology and Biochemistry, 38(3): 471-476. DOI:10.1016/j.soilbio.2005.05.019

Franchi, M., Ferris, J.P., Gallori, E., 2003. Cations as mediators of the adsorption of nucleic acids on clay surfaces in prebiotic environments. Orig Life Evol Biosph, 33(1): 1-16. DOI:10.1023/a:1023982008714

Gardner, C.M., Gunsch, C.K., 2017. Adsorption capacity of multiple DNA sources to clay minerals and environmental soil matrices less than previously estimated.

571 Chemosphere, 175: 45-51. DOI:10.1016/j.chemosphere.2017.02.030
572 Hou, Y., Wu, P., Zhu, N., 2014. The protective effect of clay minerals against damage
573 to adsorbed DNA induced by cadmium and mercury. Chemosphere, 95: 206-
574 212. DOI:10.1016/j.chemosphere.2013.08.069
575 Lajmi, A., Bourven, I., Joussein, E., Simon, S., Soubrand, M., Mehdioub, M., 2020.
576 Validation and application of diphenylamine method for DNA detection into
577 soils and clay minerals. Journal of Soils and Sediments, 20(2): 943-950.
578 DOI:10.1007/s11368-019-02427-y
579 Liang, Z., Keeley, A., 2013. Filtration Recovery of Extracellular DNA from
580 Environmental Water Samples. Environmental Science & Technology, 47(16):
581 9324-9331. DOI:10.1021/es401342b
582 Mason, J.A., Oktawiec, J., Taylor, M.K., Hudson, M.R., Rodriguez, J., Bachman, J.E.,
583 Gonzalez, M.I., Cervellino, A., Guagliardi, A., Brown, C.M., Llewellyn, P.L.,
584 Masciocchi, N., Long, J.R., 2015. Methane storage in flexible metal-organic
585 frameworks with intrinsic thermal management. Nature, 527(7578): 357-61.
586 DOI:10.1038/nature15732
587 McBride, M.B., 1994. Environmental chemistry of soils Oxford University Press. New
588 York.
589 Mikutis, G., Schmid, L., Stark, W.J., Grass, R.N., 2019. Length-dependent DNA
590 degradation kinetic model: Decay compensation in DNA tracer concentration
591 measurements. Aiche Journal, 65(1): 40-48. DOI:10.1002/aic.16433
592 Min, X., Han, P., Yang, H., Kim, H., Tong, M., 2014. Influence of sulfate and phosphate
593 on the deposition of plasmid DNA on silica and alumina-coated surfaces.
594 Colloids and Surfaces B-Biointerfaces, 118: 83-89.
595 DOI:10.1016/j.colsurfb.2014.03.039
596 Nguyen, T.H., Elimelech, M., 2007. Adsorption of plasmid DNA to a natural organic
597 matter-coated silica surface: kinetics, conformation, and reversibility. Langmuir,
598 23(6): 3273-3279.
599 Pang, L., Heiligenthal, L., Premaratne, A., Hanning, K.R., Abraham, P., Sutton, R.,
600 Hadfield, J., Billington, C., 2022. Degradation and adsorption of synthetic DNA
601 water tracers in environmental matrices. Sci Total Environ, 844: 157146.
602 DOI:10.1016/j.scitotenv.2022.157146
603 Pedreira-Segade, U., Michot, L.J., Daniel, I., 2018. Effects of salinity on the adsorption
604 of nucleotides onto phyllosilicates. Physical Chemistry Chemical Physics, 20(3):
605 1938-1952. DOI:10.1039/c7cp07004g
606 Robertson, R.M., Laib, S., Smith, D.E., 2006. Diffusion of isolated DNA molecules:
607 dependence on length and topology. Proceedings of the National Academy of
608 Sciences, 103(19): 7310-7314.
609 Saeki, K., Ihyo, Y., Sakai, M., Kunito, T., 2011a. Strong adsorption of DNA molecules
610 on humic acids. Environmental Chemistry Letters, 9(4): 505-509.
611 DOI:10.1007/s10311-011-0310-x
612 Saeki, K., Kunito, T., Sakai, M., 2010. Effects of pH, ionic strength, and solutes on
613 DNA adsorption by andosols. Biology and Fertility of Soils, 46(5): 531-535.
614 DOI:10.1007/s00374-010-0447-y

615 Saeki, K., Kunito, T., Sakai, M., 2011b. Effect of Tris-HCl Buffer on DNA Adsorption
616 by a Variety of Soil Constituents. Microbes and Environments, 26(1): 88-91.
617 DOI:10.1264/jsme2.ME10172
618 Saeki, K., Sakai, M., 2009. The Influence of Soil Organic Matter on DNA Adsorptions
619 on Andosols. Microbes and Environments, 24(2): 175-179.
620 DOI:10.1264/jsme2.ME09117
621 Sambrook, J., Fritsch, E.F., Maniatis, T., 1989. Molecular cloning: a laboratory manual.
622 Cold spring harbor laboratory press.
623 Schijven, J.F., Simunek, J., 2002. Kinetic modeling of virus transport at the field scale.
624 Journal of Contaminant Hydrology, 55(1-2): 113-35. DOI:10.1016/s0169-
625 7722(01)00188-7
626 Scholes, C.A., Millar, D.P., Gee, M.L., Smith, T.A., 2011. Resonance Energy-Transfer
627 Studies of the Conformational Change on the Adsorption of Oligonucleotides
628 to a Silica Interface. Journal of Physical Chemistry B, 115(19): 6329-6339.
629 DOI:10.1021/jp201332w
630 Sheng, X., Qin, C., Yang, B., Hu, X., Liu, C., Waigi, M.G., Li, X., Ling, W., 2019. Metal
631 cation saturation on montmorillonites facilitates the adsorption of DNA via
632 cation bridging. Chemosphere, 235: 670-678.
633 DOI:10.1016/j.chemosphere.2019.06.159
634 Šimůnek, J., van Genuchten, M.T., Sejna, M., 2008. Development and applications of
635 the HYDRUS and STANMOD software packages and related codes. Vadose
636 Zone Journal, 7(2): 587-600.
637 Sirois, S.H., Buckley, D.H., 2019. Factors governing extracellular DNA degradation
638 dynamics in soil. Environmental Microbiology Reports, 11(2): 173-184.
639 DOI:10.1111/1758-2229.12725
640 Sodnikar, K., Parker, K.M., Stump, S.R., ThomasArrigo, L.K., Sander, M., 2021.
641 Adsorption of double-stranded ribonucleic acids (dsRNA) to iron
642 (oxyhydr-)oxide surfaces: comparative analysis of model dsRNA molecules and
643 deoxyribonucleic acids (DNA). Environmental Science-Processes & Impacts,
644 23(4): 605-620. DOI:10.1039/d1em00010a
645 Vandeventer, P.E., Lin, J.S., Zwang, T.J., Nadim, A., Johal, M.S., Niemz, A., 2012.
646 Multiphasic DNA Adsorption to Silica Surfaces under Varying Buffer, pH, and
647 Ionic Strength Conditions. Journal of Physical Chemistry B, 116(19): 5661-
648 5670. DOI:10.1021/jp3017776
649 Wang, C., Hu, Z., Liu, G., Dahlke, H.E., Walter, M.T., Liu, J., Guo, L., Zhang, C., Huo,
650 Z., 2023. The advantages and disadvantages of free and encapsulated DNA
651 tracers in tracking surface and subsurface water flow and contamination. Water
652 Research, (submitted).
653 Wang, C., Liu, G., McNew, C.P., Volkmann, T.H.M., Pangle, L., Troch, P.A., Lyon, S.W.,
654 Kim, M., Huo, Z., Dahlke, H.E., 2022. Simulation of experimental synthetic
655 DNA tracer transport through the vadose zone. Water Research, 223: 119009.
656 DOI:10.1016/j.watres.2022.119009
657 Wang, C., McNew, C.P., Lyon, S.W., Walter, M.T., Volkman, T.H.M., Abramson, N.,

Sengupta, A., Wang, Y., Meira Neto, A.A., Pangle, L., Troch, P.A., Kim, M., Harman, C., Dahlke, H.E., 2019. Particle tracer transport in a sloping soil lysimeter under periodic, steady state conditions. Journal of Hydrology, 569: 61-76. DOI:10.1016/j.jhydrol.2018.11.050

Xue, J., Feng, Y., 2018. Determination of adsorption and desorption of DNA molecules on freshwater and marine sediments. Journal of Applied Microbiology, 124(6): 1480-1492. DOI:10.1111/jam.13739

Yaws, C.L., 2009. Chapter 13 - Diffusion Coefficient in Water – Inorganic Compounds. In: Yaws, C.L. (Ed.), Transport Properties of Chemicals and Hydrocarbons. William Andrew Publishing, Boston, pp. 594-596. DOI:https://doi.org/10.1016/B978-0-8155-2039-9.50018-1

Yu, W.H., Li, N., Tong, D.S., Zhou, C.H., Lin, C.X., Xu, C.Y., 2013. Adsorption of proteins and nucleic acids on clay minerals and their interactions: A review. Applied Clay Science, 80-81: 443-452. DOI:10.1016/j.clay.2013.06.003

Zhang, Y., Hartung, M.B., Hawkins, A.J., Dekas, A.E., Li, K., Horne, R.N., 2021. DNA Tracer Transport Through Porous Media—The Effect of DNA Length and Adsorption. Water Resources Research, 57(2). DOI:10.1029/2020wr028382

Zhao, Z.F., Berg, S.J., Illman, W.A., Qi, Y.C., 2022. Improving predictions of solute transport in a laboratory sandbox aquifer through high-resolution characterization with hydraulic tomography. Journal of Hydrology, 615. DOI:10.1016/j.jhydrol.2022.128673